Amorphous SnO$_2$/graphene aerogel nanocomposites harvesting superior anode performance for lithium energy storage

Linlin Fan [a,b,1], Xifei Li [a,*], Bo Yan [a,1], Xiaojia Li [a,1], Dongbin Xiong [a,1], Dejun Li [a,*], Hui Xu [c], Xianfa Zhang [c], Xueliang Sun [d,a,*]

[a] Energy & Materials Engineering Centre, College of Physics and Materials Science, Tianjin Normal University, Tianjin 300387, China
[b] National Key Laboratory of Power Sources, Tianjin Institute of Power Sources, Tianjin 300381, China
[c] Key Laboratory of Functional Inorganic Material Chemistry, Ministry of Education & School of Chemistry and Material Science, Heilongjiang University, Harbin 150080, China
[d] Nanomaterials and Energy Lab, Department of Mechanical and Materials Engineering, Western University, London, Ontario N6A 5B9, Canada

HIGHLIGHTS

- The amorphous SnO$_2$/graphene aerogel were successfully synthesized.
- The nanocomposites showed high reversible capacity and cycling stability.
- The study exhibited an effective strategy for anode materials of LIBs.

GRAPHICAL ABSTRACT
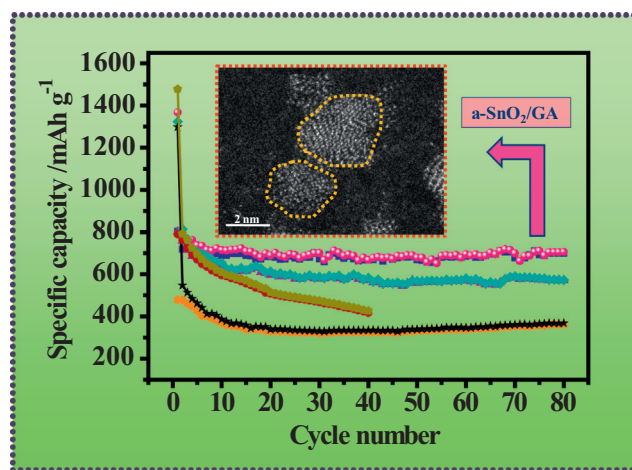
ARTICLE INFO

ABSTRACT

The Sn-based materials have been hindered from practical use for lithium ion batteries due to the inherent volume change leading to poor cycling performance. To mitigate this challenge, in this study, amorphous SnO$_2$/graphene aerogel nanocomposites are fabricated via a simple hydrothermal approach. The amorphous nature of SnO$_2$ is clearly determined in detail by transmission electron microscopy, aberration-corrected scanning transmission electron microscopy, and X-ray diffraction measurement. The as-prepared material shows satisfying reversible capacity and significant cyclic stability. For instance, it delivers an excellent discharge capacity of 700.1 mA h g^{-1} in 80th cycle at a current density of 100 mA g^{-1}, in accordance with a high retention capacity of 97.6% compared to that of the sixth cycles, which is much better than crystalline SnO$_2$/graphene aerogel. The enhanced electrochemical performance can be ascribed to the intrinsic isotropic nature, smaller size, and high electrochemical reaction kinetics of amorphous SnO$_2$, together with the graphene aerogels matrix. Therefore, this study may provide an effortless, economic, and environmental friendly strategy to fabricate high volume change electrode materials for lithium ion batteries.

© 2016 Elsevier Ltd. All rights reserved.

* Corresponding authors at: Energy & Materials Engineering Centre, College of Physics and Materials Science, Tianjin Normal University, Tianjin 300387, China (X. Li). Tel.: +86 22 23766526; fax: +86 22 23766503.
   E-mail addresses: xfli2011@hotmail.com (X. Li), dejunli@mail.tjnu.edu.cn (D. Li), xsun9@uwo.ca (X. Sun).
[1] Tel.: +86 22 23766526; fax: +86 22 23766503.

1. Introduction

Rechargeable lithium ion batteries (LIBs) emblematize state-of-the-art technology in the field of the electrochemical energy storage systems because of high energy density and good electrochemical cycling performance [1,2]. For a long time, LIBs have received great attention for energy storage applications, such as portable consumer electronics (smartphones, camera and tablet computers), power tools (electric vehicles and hybrid electric vehicles) [3–5]. Unfortunately, the LIB development for these applications is still full of challenges since the issues such as costs, safety, materials availability, and environmental friendly are addressed [6]. Especially, although graphite has been ubiquitously employed as a commercial anode material, and it is expected to play a key role in the coming process of manufacturing advanced LIBs due to good cycling performance, however, its relatively low specific capacity of $372\ mA\ h\ g^{-1}$, limited rate capability, and low density obstruct the development of LIBs [7,8]. So far, to circumvent these hurdles, metal, metal oxides, and a number of other potential materials with high theoretical reversible capacities, abundance, and non-toxic have recently received increasing attention as alternative anode materials for rechargeable LIBs, for instance, Si [9,10], Sn [11,12], SnO_2 [13], Co_3O_4 [14]. SnO_2 is a *n*-type wide-bandgap (E_g = 3.6 eV) semiconductor [15], because of relatively high theoretical capacity ($782\ mA\ h\ g^{-1}$) according to 4.4 Li per molecule and safe lithiation potential [16,17], SnO_2 has been supposed to one of the most promising electrode materials for LIBs. However, it suffers a severe capacity fading originating from its severe aggregation, poor electrical conductivity, and volume expansion during the processes of Li^+ insertion/extraction [13].

To mitigate the aforementioned challenges, one effective strategy has been proposed to conduct the SnO_2 based nanocomposites. The matrix in the composite anodes reveals high electrical conductivity as well as great tolerance of volume change [18,19]. In view of this point, various carbon-based materials such as carbon nanotubes, graphene, and porous carbon are effective candidates enhancing battery performance of SnO_2 anode. Notably, due to high surface area of over $2600\ m^2\ g^{-1}$, conductance quantization, remarkable structural flexibility, ultrashort pathway for Li^+, and excellent electrical conductivity [20–22], graphene have been receiving tremendous attention recently. For instance, the synthesized flexible nitrogen-doped graphene/SnO_2 foams [23], the dually fixed SnO_2 nanoparticles on graphene nanosheets by polyaniline coating [24], and the designed SnO_2-reduced graphene oxide composites [25] all show enhanced electrochemical performance as anodes in LIBs. More strikingly, it's generally known that amorphous nanoparticles own intrinsic isotropic nature, which can effectively buffer volume changes upon cycling [26,27], guaranteeing the integrity of the structure and excellent electrochemical performance. For instance, amorphous porous TiO_2@nitrogen doped graphene nanocomposites were designed to deliver outstanding high rate performance, e.g., $182.7\ mA\ h\ g^{-1}$ (the current density is $3.36\ A\ g^{-1}$) in 100th cycle [28]. Furthermore, McDowell et al. have illustrated that amorphous silicon compared to the crystalline can resist more efficiently the large volume modifications at least for spheres with 870 nm of diameter [29]. Based on above results, it is expected that amorphous SnO_2 based nanocomposites could minimize the effect of volume expansion during discharge–charge processes and improve the lithium energy storage.

Hence, in this study, we rationally proposed a facile strategy for the fabrication of amorphous SnO_2/graphene aerogel nanocomposites via a hydrothermal approach. Intriguingly, benefiting from the synergistic effects of intrinsic isotropic nature of amorphous SnO_2 as well as good matrix of graphene aerogels, the resultant amorphous SnO_2/graphene aerogel nanocomposites exhibit excellent electrochemical performance and great potential application when employed as anode materials for LIBs. For instance, it maintains a high energy capacity of $700.1\ mA\ h\ g^{-1}$ in the 80th discharge cycle, which corresponds to 97.6% of the 6th discharge capacity. To the best of our knowledge, this value is amongst the better published in the literature, and the synthetic strategy can be an effective access for the synthesis of carbon-based metal oxides with controlled amorphous structure.

2. Experiments

2.1. Synthesis of the amorphous and crystalline SnO_2/graphene aerogel nanocomposites

Graphene oxide (marked GO) was first synthesized using the Hummers method, as previously reported by our group [30]. SnO_2/graphene aerogel (SnO_2/GA) nanocomposites were synthesized by a facile hydrothermal method using $SnCl_2·2H_2O$ (Tianjin Fengchuan Chemical Reagent Science And Technology Co., Ltd. ⩾98.0%) as a precursor and GAs as a carrier. Specifically, 39 mg GO in 60 ml ethylene glycol (EG, Tianjin Jiangtian Chemical Technology Co., Ltd.) was dissolved in a beaker, followed by 30 min intense ultrasonication. After that, 60 mg $SnCl_2·2H_2O$ dispersed in 60 ml EG was mixed with the GO contained-solution using peristaltic pump to form a uniform mixture. Then, the resulting solution was transferred to three 50 mL Teflon-lined stainless steel autoclaves and kept at 160 °C for 1.5 h. The products were obtained via centrifuging and sequentially washing with deionized water and ethanol for several times, and then freeze-dried. Finally, amorphous SnO_2/GA (a-SnO_2/GA) nanocomposites were obtained, while, crystalline SnO_2/GA (c-SnO_2/GA) nanocomposites were synthesized by calcination at 400 °C for 4 h under Ar atmosphere. Pristine GAs were produced via the same process as for a-SnO_2/GA except that no $SnCl_2·2H_2O$ was added. Additionally, for comparison, the bare SnO_2 was synthesized by a facile reflux method. $SnCl_2·2H_2O$ was dissolved in 50 mL ethanol, followed stirring for 30 min. Subsequently, the mixed solution was transferred to the three flask filled with distilled water drop by drop, and stirred at 100 °C for 12 h with the reflux. The resultant gel was rinsed by ethanol and deionized water using a centrifuge. The final product was dried at 80 °C for 12 h, and the products were synthesized by subsequent calcination at 500 °C for 3 h in a muffle furnace.

2.2. Physical characterization

The X-ray diffraction patterns (XRD, DX-2700) of the products were obtained with CuK$_\alpha$ radiation in a coupled 2θ mode at room temperature. The results were recorded at the range of 10–80°. The morphology and structure of products were characterized with scanning electron microscope (SEM, SU8010, Hitachi), transmission electron microscope (TEM, JEOL JEM-3000F), and aberration-corrected scanning transmission electron microscopy (STEM, JEOL ARM200F, Tokyo, Japan). The microscope was equipped with a CEOS probe aberration corrector (CEOS, Heidelberg, Germany). The binding characteristics of the materials were conducted via X-ray photoelectron spectroscopy (XPS, VG ESCALAB MK II) analysis. The graphene contents in the composites were performed via thermogravimetric analysis (TGA, Pyris Diamond6000 TG/DTA, PerkinElmer Co, America) at air ranging from room temperature to 800 °C. Raman spectra were recorded on LabRAM HR800.

2.3. Electrochemical performance

Electrochemical testing was evaluated with the coin cells (CR2032), they were assembled in a glove box filled argon, where
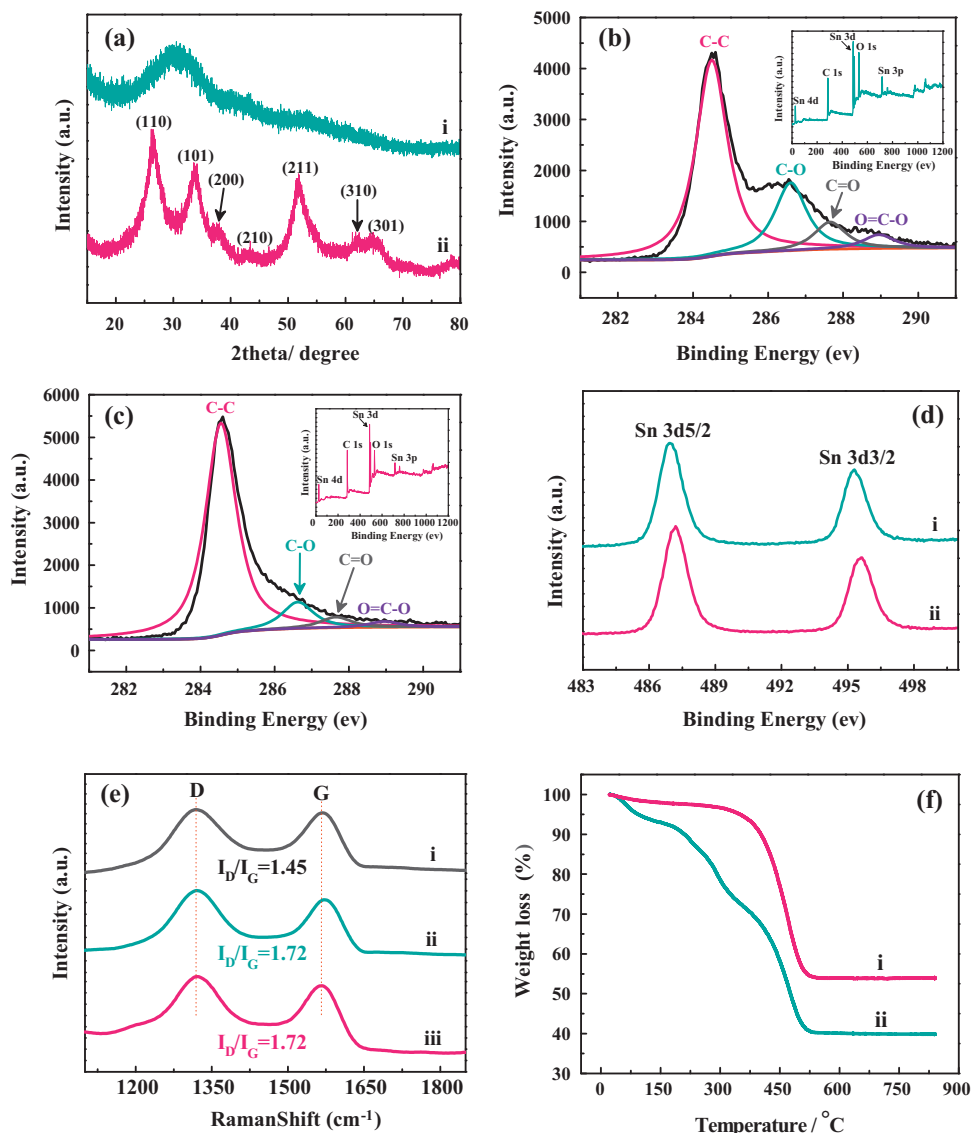
Fig. 1. (a) XRD patterns of (i) a-SnO$_2$/GA and (ii) c-SnO$_2$/GA; XPS analysis: C 1s spectra of (b) a-SnO$_2$/GA and (c) c-SnO$_2$/GA (the inset is the survey spectrum), (d) Sn 3d spectra of (i) a-SnO$_2$/GA and (ii) c-SnO$_2$/GA; (e) Raman spectra of (i) pristine GAs, (ii) a-SnO$_2$/GA, and (iii) c-SnO$_2$/GA; (f) TGA curves of (i) c-SnO$_2$/GA and (ii) a-SnO$_2$/GA.

Table 1
The C species area% of the samples based on XPS results.

	C—C 284.7 eV (%)	C—O 286.4 eV (%)	C=O 287.8 eV (%)	O—C=O 289.0 eV (%)
a-SnO$_2$/GA	65	22	8	5
c-SnO$_2$/GA	81	11	5	3

the oxygen and moisture contents were kept below 0.1 ppm. To obtain working electrodes, typically, active materials (80%), polyvinylidene fluoride (10%), and conductive carbon black (10%) were mixed in N-methyl-2-pyrrolidinone (NMP) solvent to form an uniform slurry and pasted onto Cu foil. Afterwards, they were dried at 80 °C for 12 h via a vacuum oven. Then, the electrodes were punched into 12 mm disks in diameter, and the typical electrode loading was about 0.65 mg cm^{-2}. All the cells were galvanostatically discharged and charged ranging from 0.01 V to 3.0 V using the multi-channel Land battery test system (LANHE CT2001A). Cyclic voltammetry (CV) testing data were recorded by the Princeton Applied Research VersaSTAT4 at a scan rate of

0.1 mV s^{-1} in the voltage range of 0.01–3.0 V. The electrochemical impedance spectra (EIS) were measured in a frequency range from 100 kHz to 0.01 Hz with ac signal amplitude of 5 mV. All electrochemical characterizations were performed at room temperature.

3. Results and discussion

The phase structures of a-SnO$_2$/GA and c-SnO$_2$/GA are inspected by XRD. It can be seen from Fig. 1(a) that all the diffraction peaks of c-SnO$_2$/GA are in good accordance with the standard diffraction data of rutile structure of SnO$_2$ (cassiterite, JCPDS No. 41-1445). Notably, there is no characteristic peak in a-SnO$_2$/GA except for the broad peak around 29–31°, confirming a typical nature of amorphous SnO$_2$ successfully designed onto GAs. X-ray photoelectron spectroscopy (XPS) provides the chemical composition of a-SnO$_2$/GA in comparison to c-SnO$_2$/GA. One can see from the insets in Fig. 1(b) and (c), C, O and Sn are clearly detected, and no other elements exist in both nanocomposites. The high resolution C 1 s XPS spectra of a-SnO$_2$/GA and c-SnO$_2$/GA can be deconvolved into four peaks: 284.7 eV for graphitic carbon, 286.4 eV for carbon in
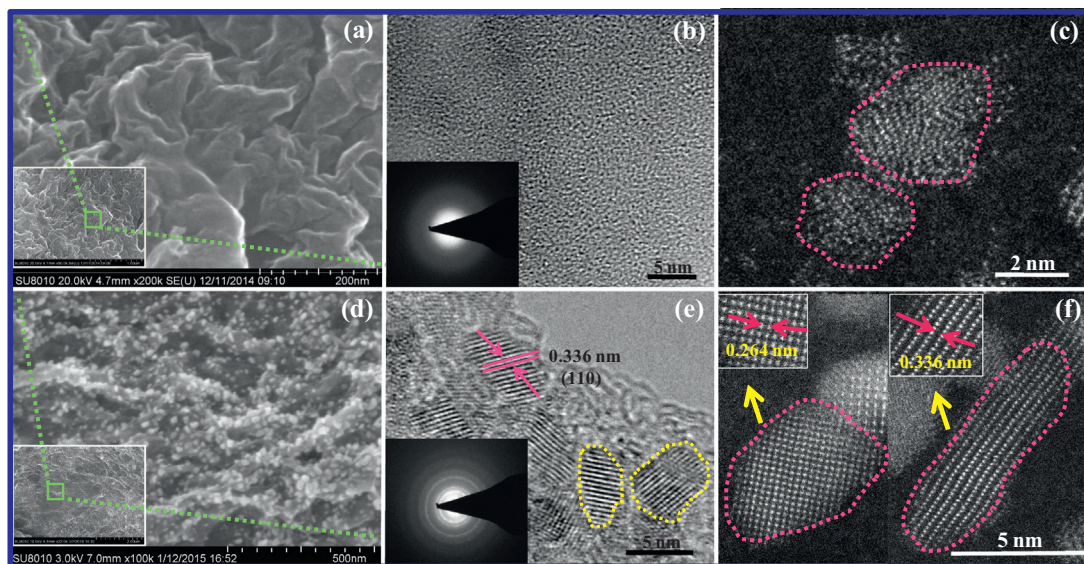
Fig. 2. Typical SEM images, HRTEM images (the inset is the SAED pattern), and high-resolution HAADF-STEM images of (a–c) a-SnO$_2$/GA and (d–f) c-SnO$_2$/GA, respectively.

epoxide groups (including C—O—C and C—OH), 287.9 eV for carbonyl carbon, 289.0 eV for carboxylate carbon [31]. Meanwhile, we quantify the peak area% in the C 1 s spectra of a-SnO$_2$/GA and c-SnO$_2$/GA, the values are presented in Table 1. Clearly, one can see that the total area% of oxygen-containing functional groups in a-SnO$_2$/GA and c-SnO$_2$/GA are estimated to be 35% and 19%, respectively, confirming that the GAs in c-SnO$_2$/GA are further reduced after annealing process [32,33]. In Fig. 1(d), a pair of peaks of Sn 3d spectra appear at 495.8 and 487.0 eV associated with Sn 3d 3/2 and Sn 3d 5/2 spinorbit peaks of SnO$_2$, demonstrating the formation of SnO$_2$ nanoparticles in the composites [34]. As seen in Fig. 1(e), the Raman spectra of pristine GAs, a-SnO$_2$/GA, and c-SnO$_2$/GA show two peaks at 1348 cm^{-1} and 1602 cm^{-1}, which are in good agreement with D band causing by defects attributed to grain boundaries, amorphous carbon species, and vacancies as well as G band caused by the presence of graphitic carbon, respectively [35–37]. Compared to the pristine GAs, both SnO$_2$/GA exhibit an increased intensity ratio (I_D/I_G), originating from a decrease of the size of sp^2 domains and the defects generated by the insertion of SnO$_2$ nanoparticles into GAs [38,39]. Thermogravimetric analysis (TGA) is employed to measure the SnO$_2$ contents in a-SnO$_2$/GA and c-SnO$_2$/GA (Fig. 1(f)). The initial weight loss is associated with the desorption of moisture. According to the weight loss of GAs, the contents of SnO$_2$ in a-SnO$_2$/GA and c-SnO$_2$/GA are calculated to be 51% and 55%, respectively.

Figs. 2 and S1 show the morphology characteristics of the synthesized a-SnO$_2$/GA and c-SnO$_2$/GA by SEM, TEM, and high-resolution HAADF-STEM images. Obviously, in Fig. 2(a), the amorphous SnO$_2$ particles are homogeneously and firmly anchored on GAs matrix. Meanwhile, one can observe that the size of amorphous SnO$_2$ particles is small. In addition, it can be seen from Fig. 2(b) and (c) that no lattice fringings are found, consistent with the amorphous state of the SnO$_2$ nanoparticles. By contrast, the particle size of crystalline SnO$_2$ increases to 10–15 nm, and they are uniformly deposited on GAs matrix, as shown in Fig. 2(d). TEM and high-resolution HAADF-STEM images (see Fig. 2(e) and (f)) clearly exhibit the crystalline character of the SnO$_2$ nanoparticles. For instance, the lattice fringes with d-spacings of 0.336 nm and 0.264 nm assign to the (1 1 0) and (1 0 1) planes of SnO$_2$. Similarly, the absence of diffraction rings of SAED (see the inset of Fig. 2(b)) and the obvious concentric rings of SAED (see

the inset of Fig. 2(e)) well agree with our design of a-SnO$_2$/GA and c-SnO$_2$/GA. As a result, the intrinsic isotropic nature and the small particle size of amorphous SnO$_2$ guarantee increased electrochemical performance. For comparison, the bare SnO$_2$ nanoparticles are synthesized, and the morphology and structure are confirmed by SEM, XRD, and XPS, as shown in Figs. S2–S4.

Fig. 3(a) and (b) exhibit typical CV characteristics corresponding to the lithiation/delithiation of the a-SnO$_2$/GA and c-SnO$_2$/GA, tested in the voltage range of 0.01–3.0 V (vs. Li$^+$/Li) with a scan rate of 0.1 mV s^{-1}. Obviously, both nanocomposites show similar CV profiles. In the initial cycle, one can see a reduction peak around 0.85 V in both samples, which is consistent with the formation of the solid electrolyte interface (SEI), as well as the conversion from SnO$_2$ to Sn [33,40]. The characteristic pair of cathodic peak (at 0.05 V) and anodic peak (at 0.55 V) are assigned to reversible lithium alloying with Sn and dealloying of Li$_x$Sn reactions, respectively [25]. Additionally, another one oxidation peak at 1.31 V is observed, which is ascribed to partially reversible reactions of Li$_2$O and Sn [41]. The CV curves almost overlap together from the second cycle, suggesting that the electrochemical reactions are reversible well. Fig. 3(c) and (d) depict the discharge and charge profiles of a-SnO$_2$/GA and c-SnO$_2$/GA in the 1st, 2nd, 20th, and 80th cycles, which are measured at a current density of 100 mA g^{-1} from 0.01 V to 3.0 V at room temperature. As can be seen, the discharge capacity of first cycle reduces rapidly compared to the second cycle. In other words, a part of initial discharge capacity can be irreversible originating from electrolyte decomposition, the formation of SEI, and the irreversible conversion from SnO$_2$ and Li to Li$_2$O and Sn in lithiation process [42]. Fortunately, in the following discharge/charge cycles, a-SnO$_2$/GA maintain a higher reversible capacity and better cyclic stability compared to c-SnO$_2$/GA.

The cycling performances of pristine GAs, bare SnO$_2$, a-SnO$_2$/GA, and c-SnO$_2$/GA electrodes under a current density of 100 mA g^{-1} are compared in Fig. 3(e). As expected, GAs matrix deliver low reversible capacity and cycliability. Meanwhile, it can be seen that the bare SnO$_2$ exhibits poor cycliability, and the specific capacity falls to 420 mA h g^{-1} upon 40 cycles, which originates from large volume change of anode materials. With the help of GAs matrix, a-SnO$_2$/GA and c-SnO$_2$/GA reveal increased performance. Interestingly, one can see that the anode crystallinity significantly affects lithium storage performance of the SnO$_2$ material. Due to the sev-
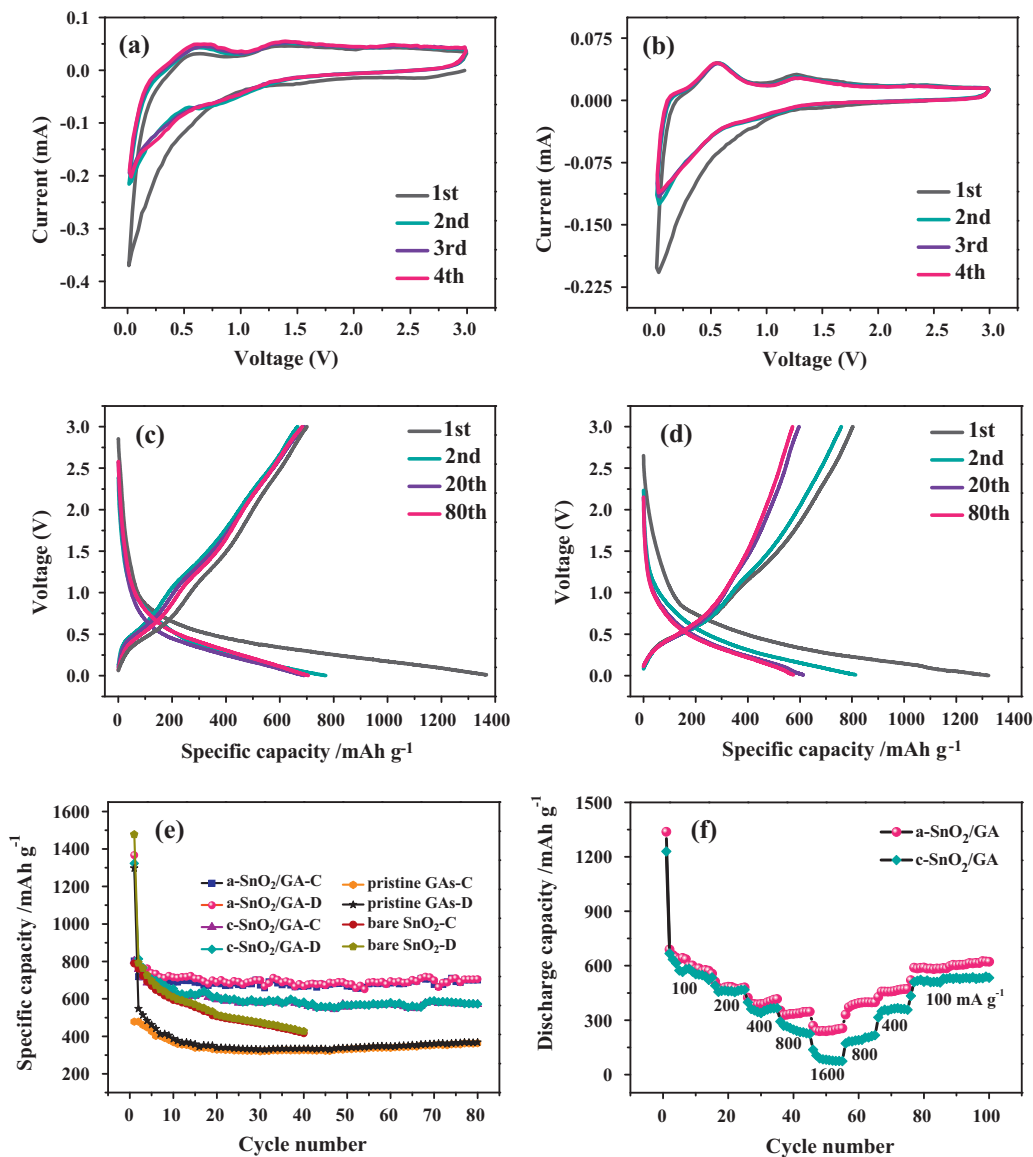
Fig. 3. The CV curves of (a) a-SnO$_2$/GA and (b) c-SnO$_2$/GA at a scan rate of 0.1 mV s^{-1} in the voltage range of 0.01–3.0 V; The discharge/charge profiles of (c) a-SnO$_2$/GA and (d) c-SnO$_2$/GA in the 1st, 2nd, 20th, and 80th cycles; (e) Comparison of the cyclic performance of pristine GAs, bare SnO$_2$, a-SnO$_2$/GA, and c-SnO$_2$/GA at a current density of 100 mA g^{-1}; (f) Rate capability of a-SnO$_2$/GA and c-SnO$_2$/GA at various current densities: 100, 200, 400, 800, 1600 mA g^{-1}.

ere volume expansion, c-SnO$_2$/GA exhibit high capacity fade. Its discharge capacity only remains 571.6 mA h g^{-1} in 80th cycle, and capacity retention is about 84% compared to that of the 6th cycle. By contrast, a-SnO$_2$/GA show enhanced cycling performance. For instance, the discharge capacity decreases to 716.6 mA h g^{-1} in the first six cycles. After that, it remains stable at around 700.1 mA h g^{-1} when the test is prolonged to 80 cycles, in accordance with a high retention rate of 97.6%. These results illustrate that the amorphous SnO$_2$ particles with the smaller size and isotropic nature demonstrate better function to relieve the volume expansion/shrinkage and make less active material lose electrical contact with the matrix, guaranteeing the excellent lithium energy storage. In order to further highlight the advantages of a-SnO$_2$/GA, the rate capability of the nanocomposites is tested using different current densities between 100 and 1600 mA g^{-1}. Clearly, we can see from Fig. 3(f) that the a-SnO$_2$/GA exhibit high reversible capacities of 689.7, 512.4, 424.5, 353.1 and 269 mA h g^{-1} at the different current densities of 100, 200, 400, 800 and 1600 mA g^{-1}, respectively. However, the specific capacities of a-SnO$_2$/GA at low current

densities (such as 100 and 200 mA g^{-1}) are comparable to that of c-SnO$_2$/GA electrode. With increased current densities at 400, 800, 1600 mA g^{-1}, a-SnO$_2$/GAs deliver higher reversible capacities than c-SnO$_2$/GA (see Fig. S5). These results clearly demonstrate the significant advantages of designed a-SnO$_2$/GA used as anode material for LIBs.

Fig. 4(a) and (b) display the electrochemical impedance spectroscopy of a-SnO$_2$/GA and c-SnO$_2$/GA in the 1st, 5th, and 10th cycles. The equivalent circuit in Fig. 4(c) is employed to simulate the obtained EIS results. Note that both SnO$_2$/GA exhibit a depressed semicircle and an angled straight line corresponding to the high frequency and low frequency range. These features are characteristic of charge transfer resistance (R_{ct}) and Warburg impedance (Z_W) of Li ions [43]. Additionally, the R_{ct} values of a-SnO$_2$/GA and c-SnO$_2$/GA in the 1st, 5th, 10th cycles are compared in Fig. 4(d). On one side, a-SnO$_2$/GA reveal lower R_{ct} than c-SnO$_2$/GA, suggesting high electrochemical reaction kinetics, which attributed to the Li ions insertion/extraction into the composites anodes [44]. On the other side, the R_{ct} values of both SnO$_2$/GA con-
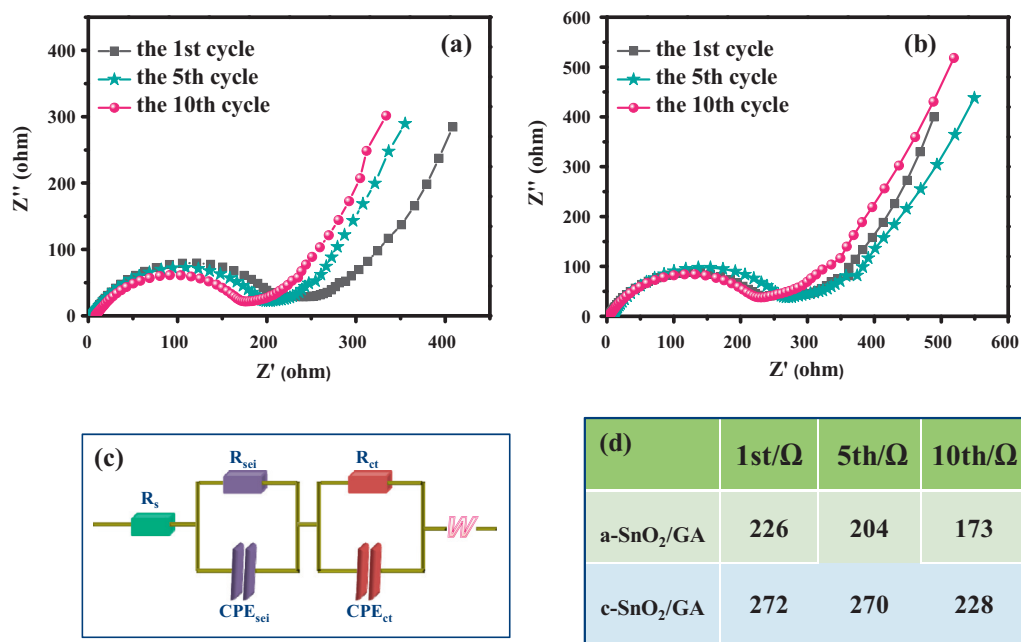
Fig. 4. The electrochemical impedance spectroscopy of (a) a-SnO$_2$/GA and (b) c-SnO$_2$/GA in the 1st, 5th, and 10th cycles; (c) The corresponding equivalent circuit used to simulate EIS curves; (d) The R_{ct} values of a-SnO$_2$/GA and c-SnO$_2$/GA in the 1st, 5th, and 10th cycles.

tinually decrease upon cycling, which confirms the enhanced electrochemical activity with increasing cycles [32,45]. Since the lithium insertion and extraction reaction rates are governed by Li$^+$ diffusion and electron conductivity, therefore, the increased electronic conductivity, that is to say, the high electrochemical reaction kinetics suggest enhanced lithium energy storage.

Based on the aforementioned discussion, we further study the morphology of a-SnO$_2$/GA after 80 charge/discharge cycles (see Fig. S6). Clearly, the a-SnO$_2$/GA structure shows some changes after repeated charge–discharge cycles to some degree. Compared to Fig. 2(b), some nanoparticles showing clear lattice fringes are observed, indicating that the resultant nanoparticles are substantially crystalline. Note that the distribution on GAs and particle size of SnO$_2$ have no obvious change, suggesting the intrinsic isotropic nature and smaller size of SnO$_2$, along with the GAs matrix can effectively relieve SnO$_2$ volume changes during charge/discharge cycles, guaranteeing the structure integrity between SnO$_2$ particles and GAs matrix. It exhibits a convincing evidence that a-SnO$_2$/GA are potential anode materials for LIBs.

4. Conclusions

In summary, LIBs have had remarkable success as power sources for portable electronic devices, on the basis of traditional graphite electrode. In our study, the designed electrode material with excellent performance is expected to be a good anode candidate. More strikingly, as more demand emerges for electrical vehicles and hybrid electric vehicles, and as emphasis shifts to the power grid and other large scale applications, exploring potential materials with high reversible capacity and high stability as alternative anode materials is eager. However, these materials show poor performance resulting from large volume change. Our results demonstrate that the amorphous nature of electrode materials can efficiently overcome this challenge, and enhance cycling performance. Hence, this study opens an excellent approach to improve electrochemical performance of electrode materials with large volume change for energy storage systems.

Appendix A. Supplementary material

Supplementary data associated with this article can be found, in the online version, at http://dx.doi.org/10.1016/j.apenergy.2016.02.094.

References

[1] Li X, Choe SY, Joe WT. A reduced order electrochemical and thermal model for a pouch type lithium ion polymer battery with LiNi$_x$Mn$_y$Co$_{1-x-y}$O$_2$/LiFePO$_4$ blended cathode. J Power Sources 2015;294:545–55.

[2] Yang F, Xing Y, Wang D, Tsui K-L. A comparative study of three model-based algorithms for estimating state-of-charge of lithium-ion batteries under a new combined dynamic loading profile. Appl Energy 2016;164:387–99.

[3] Birrozzi A, Maroni F, Raccichini R, Tossici R, Marassi R, Nobili F. Enhanced stability of SnSb/graphene anode through alternative binder and electrolyte additive for lithium ion batteries application. J Power Sources 2015;294:248–53.

[4] Burgos-Mellado C, Orchard ME, Kazerani M, Cárdenas R, Sáez D. Particle-filtering-based estimation of maximum available power state in Lithium-Ion batteries. Appl Energy 2016;161:349–63.

[5] Abdel Monem M, Trad K, Omar N, Hegazy O, Mantels B, Mulder G, et al. Lithium-ion batteries: evaluation study of different charging methodologies based on aging process. Appl Energy 2015;152:143–55.

[6] Scrosati B, Garche J. Lithium batteries: status, prospects and future. J Power Sources 2010;195:2419–30.

[7] Gómez-Cámer JL, Thuv H, Novák P. Electrochemical study of Si/C composites with particulate and fibrous morphology as negative electrodes for lithium-ion batteries. J Power Sources 2015;294:128–35.

[8] Jaguemont J, Boulon L, Dubé Y. A comprehensive review of lithium-ion batteries used in hybrid and electric vehicles at cold temperatures. Appl Energy 2016;164:99–114.

[9] Adpakpang K, Park JE, Oh SM, Kim SJ, Hwang SJ. A magnesiothermic route to multicomponent nanocomposites of $FeSi_2@Si/graphene$ and $FeSi_2@Si$ with promising anode performance. Electrochim Acta 2014;136:483–92.

[10] Chen W, Fan Z, Dhanabalan A, Chen C, Wang C. Mesoporous silicon anodes prepared by magnesiothermic reduction for lithium ion batteries. J Electrochem Soc 2011;158:A1055–9.

[11] Hou X, Hu Y, Jiang H, Li Y, Niu X, Li C. $Sn@Ni_3Sn_4$ embedded nanocable-like carbon hybrids for stable lithium-ion batteries. Chem Commun (Cambridge, England) 2015;51:16373–6.

[12] Lubke M, Johnson I, Makwana NM, Brett D, Shearing P, Liu ZL, et al. High power TiO_2 and high capacity Sn-doped TiO_2 nanomaterial anodes for lithium-ion batteries. J Power Sources 2015;294:94–102.

[13] Yang Q, Zhao JC, Sun T, Yu JY. Enhanced performance of SnO_2–C composite fibers containing NiO as lithium-ion battery anodes. Ceram Int 2015;41:11213–20.

[14] Pan GX, Xia XH, Cao F, Chen J, Zhang YJ. Construction of Co/Co_3O_4–C ternary core-branch arrays as enhanced anode materials for lithium ion batteries. J Power Sources 2015;293:585–91.

[15] Yang H, Yu G, Liu H. Synthesis of 3D flower-like SnO_2 with hierarchical nanostructure and high reversible capacity as lithium-ion battery anode. J Electron Mater 2015;44:3744–51.

[16] Derrien G, Hassoun J, Panero S, Scrosati B. Nanostructured Sn–C composite as an advanced anode material in high-performance lithium-ion batteries. Adv Mater 2007;19:2336–40.

[17] Lou XW, Li CM, Archer LA. Designed synthesis of coaxial $SnO_2@carbon$ hollow nanospheres for highly reversible lithium storage. Adv Mater 2009;21:2536–9.

[18] Yang ZS, Chen CY, Liu CW, Chang HT. Electrocatalytic sulfur electrodes for CdS/CdSe quantum dot-sensitized solar cells. Chem Commun 2010;46:5485–7.

[19] Yu Y, Yang Q, Teng D, Yang X, Ryu S. Reticular Sn nanoparticle-dispersed PAN-based carbon nanofibers for anode material in rechargeable lithium-ion batteries. Electrochem Commun 2010;12:1187–90.

[20] Li M, Li X, Li W, Meng X, Yu Y, Sun X. Atomic layer deposition derived amorphous TiO_2 thin film decorating graphene nanosheets with superior rate capability. Electrochem Commun 2015;57:43–7.

[21] Wang X, Zhou X, Yao K, Zhang J, Liu Z. A $SnO_2/graphene$ composite as a high stability electrode for lithium ion batteries. Carbon 2011;49:133–9.

[22] Zhao Y, Li X, Yan B, Li D, Lawes S, Sun X. Significant impact of 2D graphene nanosheets on large volume change tin-based anodes in lithium-ion batteries: a review. J Power Sources 2015;274:869–84.

[23] Cong HP, Xin S, Yu SH. Flexible nitrogen-doped graphene/SnO_2 foams promise kinetically stable lithium storage. Nano Energy 2015;13:482–90.

[24] Dong Y, Zhao Z, Wang Z, Liu Y, Wang X, Qiu J. Dually fixed SnO_2 nanoparticles on graphene nanosheets by polyaniline coating for superior lithium storage. ACS Appl Mater Interfaces 2015;7:2444–51.

[25] Li W, Yoon D, Hwang J, Chang W, Kim J. One-pot route to synthesize SnO_2-reduced graphene oxide composites and their enhanced electrochemical performance as anodes in lithium-ion batteries. J Power Sources 2015;293:1024–31.

[26] Lin YM, Abel PR, Flaherty DW, Wu J, Stevenson KJ, Heller A, et al. Morphology dependence of the lithium storage capability and rate performance of amorphous TiO_2 electrodes. J Phys Chem C 2011;115:2585–91.

[27] Arthur TS, Kato K, Germain J, Guo JH, Glans P, Liu YS, et al. Amorphous V_2O_5–P_2O_5 as high-voltage cathodes for magnesium batteries. Chem Commun 2015;51:15657–60.

[28] Li S, Xue P, Lai C, Qiu J, Ling M, Zhang S. Pseudocapacitance of amorphous $TiO_2@nitrogen$ doped graphene composite for high rate lithium storage. Electrochim Acta 2015;180:112–9.

[29] McDowell MT, Lee SW, Harris JT, Korgel BA, Wang C, Nix WD, et al. In situ TEM of two-phase lithiation of amorphous silicon nanospheres. Nano Lett 2013;13:758–64.

[30] Li X, Hu Y, Liu J, Lushington A, Li R, Sun X. Structurally tailored graphene nanosheets as lithium ion battery anodes: an insight to yield exceptionally high lithium storage performance. Nanoscale 2013;5:12607–15.

[31] Tan C, Zhao S, Yang G, Hu S, Qin X. Facile and surfactant-free synthesis of SnO_2–graphene hybrids as high performance anode for lithium-ion batteries. Ionics 2014;21:987–94.

[32] Zhang C, Peng X, Guo Z, Cai C, Chen Z, Wexler D, et al. Carbon-coated $SnO_2/graphene$ nanosheets as highly reversible anode materials for lithium ion batteries. Carbon 2012;50:1897–903.

[33] Ye F, Zhao B, Ran R, Shao Z. Facile mechanochemical synthesis of nano $SnO_2/graphene$ composite from coarse metallic Sn and graphite oxide: an outstanding anode material for lithium-ion batteries. Chem-Eur J 2014;20:4055–63.

[34] Yang S, Yue W, Zhu J, Ren Y, Yang X. Graphene-based mesoporous SnO_2 with enhanced electrochemical performance for lithium-ion batteries. Adv Funct Mater 2013;23:3570–6.

[35] Du N, Wu X, Zhai C, Zhang H, Yang D. Large-scale synthesis and application of SnS_2–graphene nanocomposites as anode materials for lithium-ion batteries with enhanced cyclic performance and reversible capacity. J Alloys Compd 2013;580:457–64.

[36] Zhao B, Zhang G, Song J, Jiang Y, Zhuang H, Liu P, et al. Bivalent tin ion assisted reduction for preparing graphene/SnO_2 composite with good cyclic performance and lithium storage capacity. Electrochim Acta 2011;56:7340–6.

[37] Chen Y, Wang J, Liu H, Banis MN, Li R, Sun X, et al. Nitrogen doping effects on carbon nanotubes and the origin of the enhanced electrocatalytic activity of supported Pt for proton-exchange membrane fuel cells. J Phys Chem C 2011;115:3769–76.

[38] Liu S, Lu X, Xie J, Cao G, Zhu T, Zhao X. Preferential c-axis orientation of ultrathin SnS_2 nanoplates on graphene as high-performance anode for Li-ion batteries. ACS Appl Mater Interfaces 2013;5:1588–95.

[39] Chen P, Su Y, Liu H, Wang Y. Interconnected tin disulfide nanosheets grown on graphene for Li-ion storage and photocatalytic applications. ACS Appl Mater Interfaces 2013;5:12073–82.

[40] Zhao Y, Li J, Wang N, Wu C, Dong G, Guan L. Fully reversible conversion between SnO_2 and Sn in $SWNTs@SnO_2@PPy$ coaxial nanocable as high performance anode material for lithium ion batteries. J Phys Chem C 2012;116:18612–7.

[41] Cai D, Yang T, Wang D, Duan X, Liu B, Wang L, et al. Tin dioxide dodecahedral nanocrystals anchored on graphene sheets with enhanced electrochemical performance for lithium-ion batteries. Electrochim Acta 2015;159:46–51.

[42] Zhang K, Li X, Liang J, Zhu Y, Hu L, Cheng Q, et al. Nitrogen-doped porous interconnected double-shelled hollow carbon spheres with high capacity for lithium ion batteries and sodium ion batteries. Electrochim Acta 2015;155:174–82.

[43] Etacheri V, Seisenbaeva GA, Caruthers J, Daniel G, Nedelec JM, Kessler VG, et al. Ordered network of interconnected SnO_2 nanoparticles for excellent lithium-ion storage. Adv Energy Mater 2015;5:1401289–96.

[44] Wang D, Li X, Wang J, Yang J, Geng D, Li R, et al. Defect-rich crystalline SnO_2 immobilized on graphene nanosheets with enhanced cycle performance for Li ion batteries. J Phys Chem C 2012;116:22149–56.

[45] Fan L, Li X, Cui Y, Xu H, Zhang X, Xiong D, et al. Tin oxide/graphene aerogel nanocomposites building superior rate capability for lithium ion batteries. Electrochim Acta 2015;176:610–9.